Langmuir

Article

pubs.acs.org/Langmuir

Nanoscale Interfacial Friction and Adhesion on Supported versus Suspended Monolayer and Multilayer Graphene

Zhao Deng,[†,‡] Nikolai N. Klimov,[†,§] Santiago D. Solares,[‡,∥] Teng Li,[‡,∥] Hua Xu,[†,‡] and Rachel J. Cannara*[,†]

[†]Center for Nanoscale Science and Technology and [§]Physical Measurement Laboratory, National Institute of Standards and Technology, Gaithersburg, Maryland 20899, United States

[‡]Maryland NanoCenter and [∥]Department of Mechanical Engineering, University of Maryland, College Park, Maryland 20742, United States

Supporting Information

ABSTRACT: Using atomic force microscopy (AFM), supported by semicontinuum numerical simulations, we determine the effect of tip−subsurface van der Waals interactions on nanoscale friction and adhesion for suspended and silicon dioxide supported graphene of varying thickness. While pull-off force measurements reveal no layer number dependence for supported graphene, suspended graphene exhibits an increase in pull-off force with thickness. Further, at low applied loads, friction increases with increasing number of layers for suspended graphene, in contrast to reported trends for supported graphene. We attribute these results to a competition between local forces that determine the deformation of the surface layer, the profile of the membrane as a whole, and van der Waals forces between the AFM tip and subsurface layers. We find that friction on supported monolayer graphene can be fit using generalized continuum mechanics models, from which we extract the work of adhesion and interfacial shear strength. In addition, we show that tip−sample adhesive forces depend on interactions with subsurface material and increase in the presence of a supporting substrate or additional graphene layers.

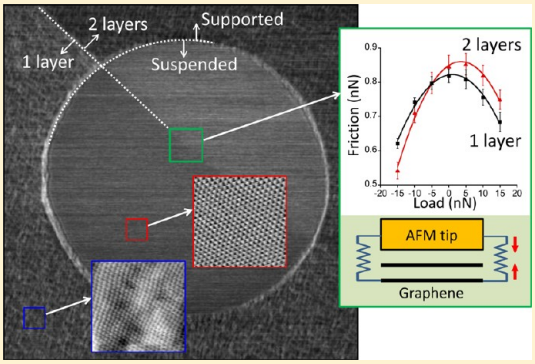

1. INTRODUCTION

Graphene has attracted broad interest for its unique electronic,[1,2] thermal,[3,4] and mechanical[5−8] properties and may be an important material for future electronics and micro- or nanoelectromechanical systems (M/NEMS).[9,10] Should graphene become a material of interest for M/NEMS, its interfacial and mechanical properties will play an important role in determining overall system performance. As a model material, an in-depth investigation leading to an improved understanding of the mechanical and interfacial behavior of graphene would advance knowledge of the mechanistic origins of friction and adhesion and potentially lead to its implementation in future M/NEMS devices.

Although graphene has been studied extensively in terms of its electronic properties and chemical modifications,[11−13] investigations of its tribological properties remain limited, both experimentally and theoretically. A few studies employing atomic force microscopy (AFM) have been carried out on the nanomechanical properties of monolayer and multilayer graphene membranes,[6−8,13−17] including the discovery that the graphene monolayer is the stiffest material measured to date, with an effective in-plane Young's modulus of approximately 1 TPa.[6] The impact of the number of layers on the frictional behavior of substrate-supported graphene has also been investigated, and a decrease of friction force with increasing thickness was observed.[7,8,18−20] This behavior was attributed to the dependence of out-of-plane deformation on the number of layers of graphene exfoliated onto a rigid substrate (silicon dioxide)[7,8] and to electron−phonon coupling for graphene grown epitaxially on silicon carbide.[18,19] Molecular dynamics (MD) simulations have qualitatively reproduced the observed thickness dependence of friction, with viscoelasticity as the primary dissipation mechanism.[21] Further, anisotropic friction on graphene has been attributed to sliding direction-dependent rippling of the exfoliated layer.[22]

To our knowledge, no study has been reported that correlates a detailed load dependence of friction with the adhesive properties of graphene. In this article, we demonstrate through experiment and simulation that frictional and adhesive properties are coupled through van der Waals interactions between the AFM tip and the graphene surface and are altered by interactions between the tip and subsurface material and the mechanical contribution of a supporting substrate.

Received: October 14, 2012
Revised: December 4, 2012
Published: December 7, 2012

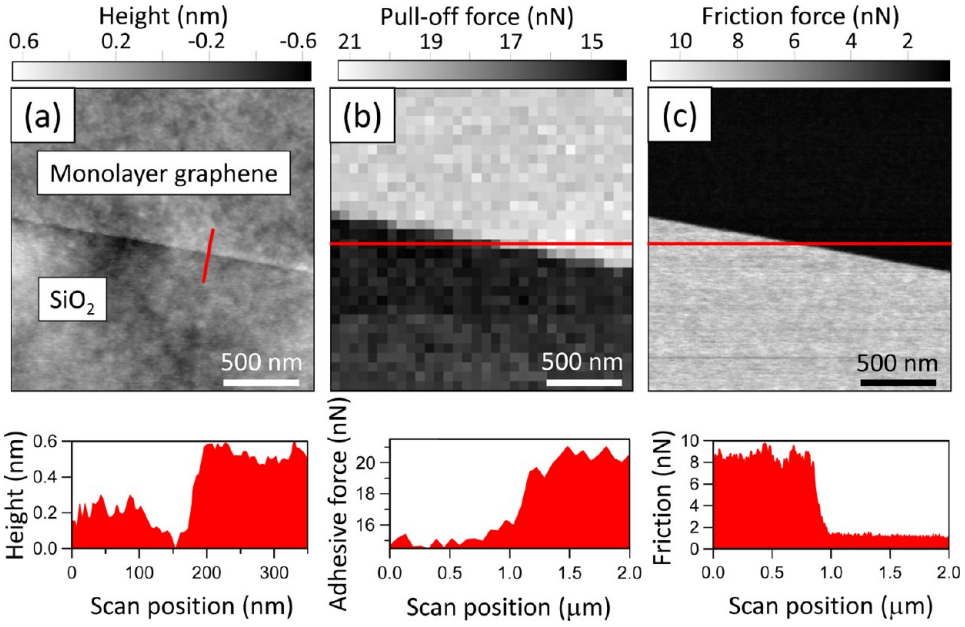

Figure 1. (a) AFM topography image and section profile along the red line in the topography showing the edge of a graphene monolayer exfoliated onto a SiO_2/Si substrate. (b) Corresponding pull-off force map and section profile along the red line in the pull-off force map for the topographical area shown in (a). (c) Corresponding friction force map and section profile along the same red line in (b) for the topographical area shown in (a).

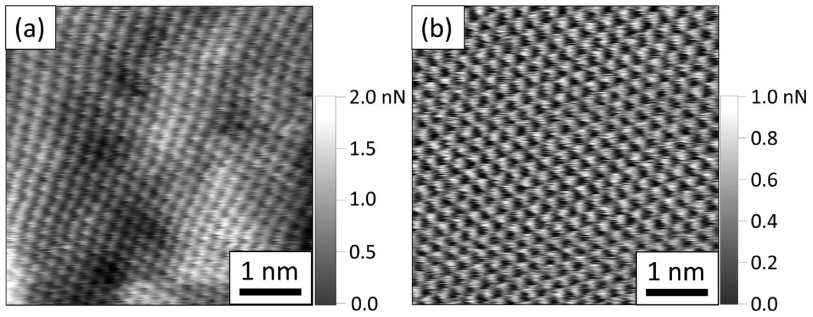

Figure 2. Stick–slip lateral force images on adjacent (a) supported and (b) suspended regions of a graphene monolayer over 5 nm scan sizes at an applied load of ≈42 nN.

2. EXPERIMENT AND SIMULATIONS

We compared supported and suspended graphene, prepared via mechanical exfoliation of natural graphite onto silicon dioxide (SiO_2) substrates patterned with arrays of 1.6 μm diameter pits, as described in detail in Section S1 of the Supporting Information. Raman spectroscopy (Supporting Information, Figure S2) confirmed the thickness of the supported and suspended graphene based on the known dependence of the G and two-dimensional (2D) Raman peaks on layer number.[14,23,24] AFM maps of topography, friction, and pull-off force were recorded over the same regions, primarily using a 15 nm radius silicon nitride (Si_3N_4) probe (Supporting Information, Section S1). Additional variable-load friction measurements were performed over nanoscale scan lines at specific locations. Loads ranged from positive (i.e., pushing into the surface) to negative (i.e., pulling on the surface) to a maximum tensile load or "pull-off" point, at which the AFM tip separates from the surface. We first characterized the adhesive and frictional behaviors of supported graphene and compared with those of the bare SiO_2 surface. We then compared these results with mono-, bi-, and trilayer suspended graphene. Details regarding the full set of AFM tips used in the experiments, as well as the calibration and measurement methods, are included in Section S1 of the Supporting Information.

To support the interpretation of the AFM results, we conducted two sets of semicontinuum numerical mechanics simulations, as described in Section S2 of the Supporting Information. In the first set (Supporting Information, Figure S4a), we calculated the pressure between a perfectly flat and infinite Si_3N_4 surface (the tip material) and a graphene layer as a function of the number of subsurface graphene layers and the presence or absence of an SiO_2 substrate. In the second set of simulations (Supporting Information, Figure S4b), we constructed an axisymmetric continuum-sheet model of a 1.6 μm diameter clamped circular graphene membrane interacting with a 15 nm radius Si_3N_4 sphere (representing the AFM tip). We then calculated the force between the tip and the membrane as a function of vertical position for membranes of different numbers of layers (n = 1, 2, and 3). These two approaches allowed us to make a qualitative assessment of the impact of subsurface material (SiO_2 vs graphene) and overall structure (supported vs suspended) on contact pressure and the applied load required to achieve a certain membrane height.

3. RESULTS

3.1. Topography, Adhesion, and Friction on Supported Graphene versus Bare SiO_2. Figure 1a shows the surface topography of the supported graphene monolayer (confirmed by Raman) and the SiO_2 surface, with a step height of (0.5 ± 0.1) nm. This value is greater than the graphene–graphene distance, consistent with previous reports.[25,26] The root-mean-square (rms) surface roughness of (0.12 ± 0.01) nm for the graphene monolayer was less than the underlying

dx.doi.org/10.1021/la304079a | Langmuir 2013, 29, 235–243

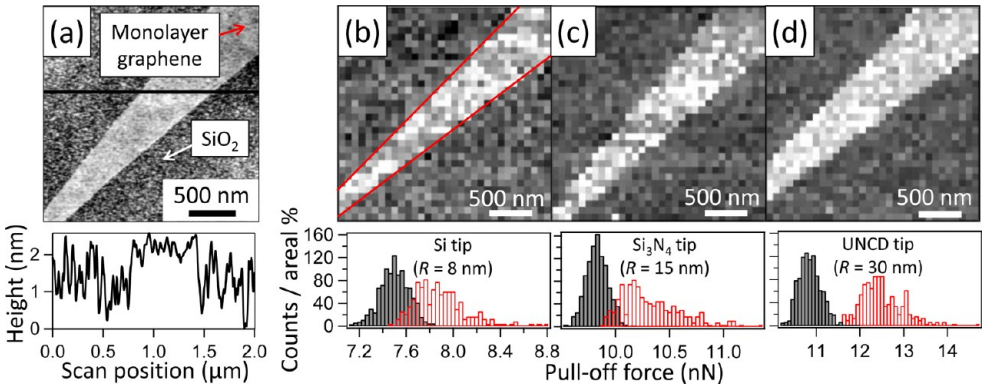

Figure 3. (a) Topography and section profile along the red line in the topography of a supported graphene monolayer. (b–d) Corresponding pull-off force maps and histograms acquired using (b) Si, (c) Si_3N_4, and (d) UNCD tips. Solid gray (lefthand data) and open red (righthand data) histograms below each map correspond to bare SiO_2 and SiO_2/Si-supported graphene areas, respectively.

substrate roughness of (0.19 ± 0.02) nm but regulated by the topography of the substrate.[27] This morphology is dictated by a competition between the corrugation-induced strain energy of the graphene and the graphene–substrate interaction energy,[28,29] an effect evident in the distorted stick–slip friction image shown in Figure 2a. Figure 2b shows the undistorted periodicity in the lattice structure of an adjacent suspended graphene monolayer.

In Figure 1b, a map of the pull-off force corresponding to the topographical area in Figure 1a shows a distinct contrast between the graphene monolayer and the SiO_2 surface. Pull-off forces, which can be rate dependent, can nonetheless reveal variations between surfaces that correspond to differences in adhesive force (when the same pulling rate is used). We found that pull-off, and thus adhesive, forces are generally higher on SiO_2/Si-supported graphene than on the bare SiO_2 surface (Figure 1b), although adhesion can vary from one location to the next and with slight changes in conditions. As shown in Figure 3b–d, the pull-off force increased with the tip radius, as expected based on an increase in contact area. Accordingly, if we invoke continuum mechanics (as justified below) and assume that the work of adhesion, W, is proportional to the pull-off force divided by the tip radius, we find that, for both supported graphene and SiO_2, W varies in decreasing order for the Si, Si_3N_4, and UNCD tips. As this opposes the observed trend in pull-off force, we can thus attribute the latter to the tip radius (i.e., the contact area). We note that we observed no rate dependence in the pull-off force measurements when comparing 1 μm/s with 5 μm/s (and ≈0.01 μm/s for the friction–load measurements).

The friction force maps produced a contrast qualitatively opposite to the pull-off force maps, as shown in Figure 1c where friction forces decreased by ≈90% on the supported monolayer relative to SiO_2. Figure 4 presents two typical friction–load curves acquired on the SiO_2/Si substrate and graphene monolayer, respectively. At high loads, the friction force on the SiO_2 surface was over 1 order of magnitude greater than friction forces measured on supported graphene. In both cases, friction–load curves fit well to an established continuum mechanics model, referred to as the Maugis–Dugdale (or "transition") model in its generalized form.[30] The transition model is used to determine the position of the interface along a spectrum of contact behavior ranging from Derjaguin–Mueller–Toporov (DMT)[31] for hard contacts or long-range interaction forces to Johnson–Kendall–Roberts (JKR)[32] for

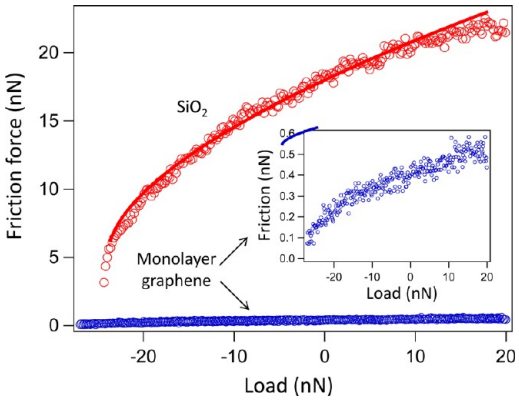

Figure 4. Representative friction–load curves acquired on the supported graphene monolayer (open blue circles) and bare SiO_2 surface (open red circles) using the Si_3N_4 tip. Inset: magnification of the supported graphene monolayer data. The solid lines are fits using the DMT–JKR transition model.

soft contacts or short-range forces.[30,33–35] The location of the contact within this generalized model is represented by the dimensionless parameter, λ, which ranges nonlinearly from zero (DMT) to infinity (JKR). In practice, however, λ is typically found to converge to values less than 10.[33] For $\lambda > 0.5$, a contact is considered to have transitioned toward the JKR regime.

We obtained λ by fitting our friction–load data using a simplified analytical solution of the transition model, developed and described elsewhere.[33,34] We compared λ for the supported graphene monolayer and SiO_2 surface based on transition fits to over 20 friction–load curves for each surface. Average λ values appear in Table 1 and indicate that, despite the relatively large standard deviations due to surface heterogeneity, both contacts tended toward the JKR end of the spectrum. Despite the contrast in pull-off force for the supported monolayer versus

Table 1. Continuum Mechanics Transition Fit Results for the Bare SiO_2 and SiO_2/Si-Supported Monolayer Graphene Surfaces

	transition parameter, λ	work of adhesion, W (J/m^2)	shear strength, τ (MPa)
bare SiO_2	0.63 ± 0.30	0.32 ± 0.05	1250 ± 200
supported monolayer	0.92 ± 0.35	0.34 ± 0.06	23.6 ± 2.3

dx.doi.org/10.1021/la304079a | Langmuir 2013, 29, 235–243

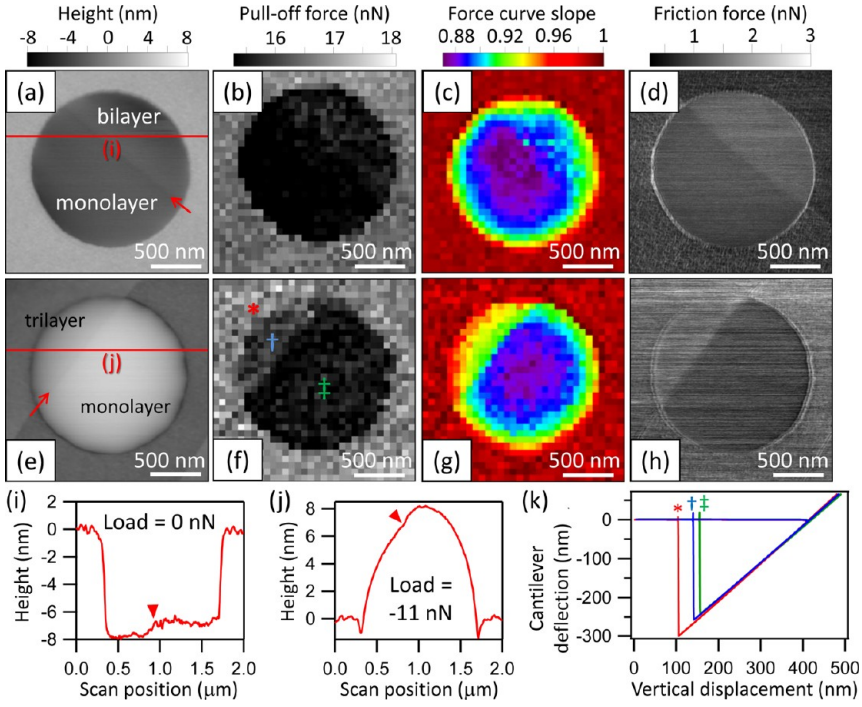

Figure 5. (a) Zero-load topographical image of a graphene membrane, with a monolayer/bilayer boundary traversing the circular pit; (b) corresponding pull-off force map; (c) corresponding map of the slopes of the force−displacement curves taken in (b); and (d) corresponding friction map (at zero applied load). (e−h) Same as (a−d) but with an applied load of −11 nN on a graphene membrane consisting of a monolayer and a trilayer. (i, j) Section profiles shown in (a) and (e), respectively. (k) Three representative vertical force−displacement curves taken on the three membrane regions, as indicated in (f). The red arrows in (a, e, i, j) indicate monolayer/multilayer boundaries.

the bare SiO_2, the transition fits yielded similar work of adhesion (W) values of ≈300 mJ/m^2 (Table 1), where we have assumed the pull-off force is the adhesive force. While pull-off forces were greater, the friction forces were lower for supported graphene relative to the SiO_2 surface because its shear strength, τ, is correspondingly lower, by a factor of ≈50. Calculated values appear in Table 1, where we have used the Young's modulus (E = 70 GPa) and Poisson's ratio (ν = 0.2) of the SiO_2 substrate for the elastic properties of the sample in both cases. (We used E = 280 GPa and ν = 0.2 for the Si_3N_4 tip.) If we instead use the bulk elastic constants of graphite (E = 30 GPa; ν = 0.24), we obtain τ = (14.4 ± 1.4) MPa for the supported monolayer. In either case, the shear strength for Si_3N_4 sliding against bare SiO_2 is 1−2 orders of magnitude greater than the supported graphene monolayer, despite their similar work of adhesion values.

3.2. Adhesion and Friction Contrast on Suspended versus Supported Graphene. We found that membranes exhibited dramatically different tribological properties in comparison with supported graphene, as they are highly flexible and more easily deformed by the AFM tip. Figure 5a shows the topography of a suspended graphene region (same as in Figure S2b of the Supporting Information), where a boundary between monolayer and bilayer graphene traverses a pit. An equilibrium depression of the membranes into the pits was observed (see also Figure S1 of the Supporting Information), in agreement with previous observations from tapping mode experiments.[6,14] In addition, we consistently found that graphene membranes attach to the sidewalls of pits, even when these membranes are imaged exclusively under negative loads (pulling forces).

In Figure 5e, a monolayer/trilayer boundary traverses a pit, demonstrating that the trilayer section of the membrane deflects less than the monolayer under a given normal load (cross section in Figure 5j). In Figure 5i (cross section from Figure 5a) and j, each plotted point is an instantaneous sample of the membrane height at the contact point; the actual shape of the membrane changes continuously during the imaging process, with the maximum deflection occurring at the position farthest from the edge of the pit.[36] Accordingly, the slopes of the force curves increase near the edge, as shown in Figure 5c,g, which also shows that thicker regions of membranes are stiffer. (The slope of a force curve represents the combined stiffness of the cantilever and membrane in the vertical direction.) In contrast, friction and pull-off forces were not position-dependent for membranes of a given thickness, showing consistency in the average local van der Waals interaction.

We observed that pull-off forces on the membranes depended on layer number (thickness) and were consistently lower than pull-off forces on supported graphene, which exhibited no observable thickness dependence (Figure 5b,f). In Figure 5b, the graphene monolayer shows the lowest pull-off forces, followed by increasingly higher pull-off forces on the bilayer membrane and supported graphene. This very slight upward trend in pull-off force with more subsurface material also occurred when comparing monolayer and trilayer membranes (Figure 5f). In general, pull-off forces on mono-, bi-, and trilayer graphene membranes decreased by (10.3 ± 0.5)%, (8.1 ± 0.2)%, and (6.0 ± 0.2)%, respectively, relative to the SiO_2/Si-supported monolayer.

Figure 5 includes simultaneous maps of the topography (Figure 5a,e) and friction force (Figure 5d,h) on supported and suspended graphene, revealing differences in tribological behavior depending on structure. Our variable-load measurements on supported graphene are consistent with previous observations that an increase in the number of graphene layers

dx.doi.org/10.1021/la304079a | Langmuir 2013, 29, 235−243

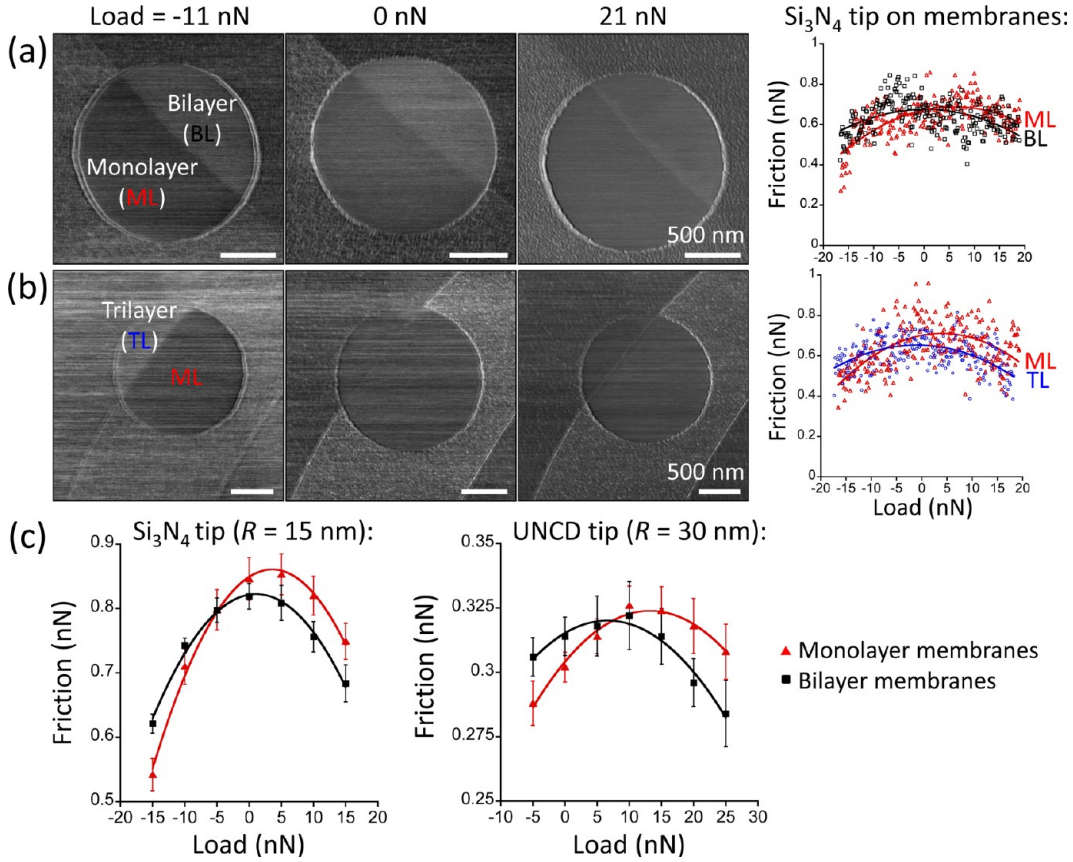

Figure 6. The maps in (a) and (b) are extracted from serial friction images at different applied normal loads on the bilayer/monolayer and trilayer/monolayer membrane regions shown in Figure 5a and e, respectively, using the Si_3N_4 tip. The data are plotted on different absolute scales for visual clarity, illustrating the crossovers in friction generally observed when comparing mono- and multilayer membranes. (All scale bars: 500 nm.) (c) Friction as a function of load for several load values (excluding pull-off), showing data obtained using the Si_3N_4 and UNCD tips. The friction values each correspond to averages from at least fifteen 10 nm sized friction−load measurements on the suspended graphene monolayer (red triangles) and bilayer (black squares) shown in (a); error bars correspond to the standard devation of the mean, and solid lines correspond to second-order polynomial fits to the data.

is accompanied by a decrease in friction force for graphene exfoliated onto SiO_2.[7,8] However, we found that this trend is not strictly followed by suspended graphene, depending on the applied load. Figure 5d shows a reversal in friction contrast between mono- and bilayer graphene membranes with respect to their supported counterparts. At low loads, although the supported graphene monolayer exhibits greater friction than the supported bilayer, the suspended monolayer exhibits reduced friction relative to its bilayer counterpart. The same trend was observed for monolayers versus trilayers (Figure 5h).

3.3. Switch of Frictional Contrast with Varying Load on Suspended Graphene. We mapped friction forces under discrete applied loads ranging from −11 to 21 nN on the two membrane regions in Figure 5a,e, as shown in Figure 6a,b, respectively. In both cases, the suspended monolayer exhibited lower friction than multilayers at low loads but similar or higher friction at high loads. Meanwhile, supported graphene showed a continuous enhancement in frictional contrast between mono- and multilayer regions with increasing load. The right-most plots in Figure 6a,b are representative plots of raw friction data taken as a function of load over 10 nm scan lines on each of the membrane regions. Similar to the pull-off force measurements (e.g., Figure 5b), the vicinity of the edge of the membrane to the position at which these local friction−load measurements were performed did not have an observable effect on measured values. In contrast to friction on supported monolayer graphene (e.g., Figure 4, inset), existing continuum mechanics models cannot be applied to suspended graphene. Instead, second-order polynomial fits serve as visual guides indicating overall trends in the data.

For suspended graphene, friction generally increased with decreasing load in the positive load regime and decreased again in the negative load regime until pull-off occurred, leading to friction−load plots with negative (downward) curvature. Figure 6c compares the mean friction force for the Si_3N_4 and UNCD tips at specific load values for the suspended monolayer versus suspended bilayer shown in Figure 6a. The friction data are average values from multiple duplicated trials at each of 5 different locations on a given membrane; that is, each of the 7 data points is an average over data at the corresponding load, extracted from 5−10 separate friction−load curves. The plots do not extend all the way to pull-off, as pull-off forces differed depending on membrane thickness (Section 3.2). Here, uncertainties in the friction−load data represent the standard deviation of the mean. While absolute differences in raw friction on monolayer versus multilayer graphene were very small, they consistently exhibited crossovers near zero load, as exemplified by Figure 6c.

3.4. Calculation of Contact Forces and Membrane Profiles. Mutual attraction between the tip and subsurface

dx.doi.org/10.1021/la304079a | *Langmuir* 2013, 29, 235−243

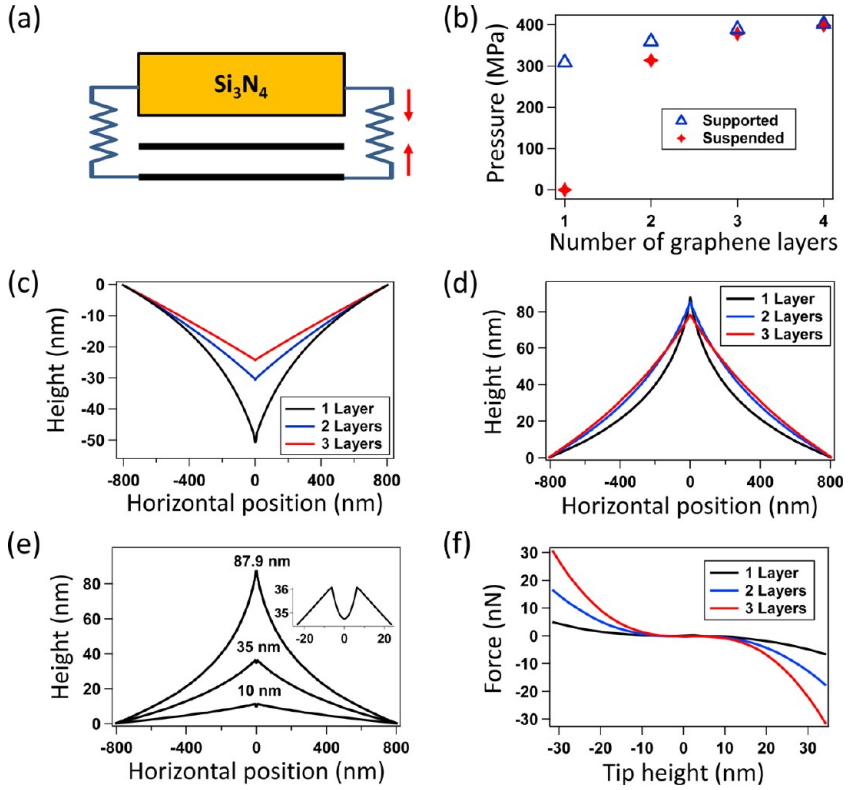

Figure 7. (a) Schematic of the compression effect on the graphene top layer due to van der Waals attraction between a subsurface layer and the AFM tip. (b) Calculated pressure between the AFM tip and the top graphene layer for the supported and suspended cases for different numbers of graphene layers. (c) Calculated profiles for membranes of different thickness under the application of a 15 nN downward force by the AFM tip. (d) Calculated membrane profiles for different numbers of layers at the maximum height attained while being pulled upward by the AFM tip; corresponding loads were ≈65 nN (monolayer), ≈200 nN (bilayer), and ≈300 nN (trilayer). (e) Calculated profile for a monolayer membrane for three different tip heights (the inset shows a close-up of the area around the AFM tip for a tip height of 35 nm). (f) Calculated force vs tip height for different thicknesses.

graphene layers or SiO_2/Si substrate can compress the surface layer against the tip, as illustrated in Figure 7a. As a consequence of tip−subsurface material attraction, we found that contact pressures were compressive in all cases except for the suspended monolayer, where the pressure can vanish at 0 K if the surface is perfectly flat. Figure 7b shows that the compressive stress due to subsurface layers increases with layer number (thickness), and this trend is much steeper for the suspended case than for the supported case; in the suspended case, the addition of subsurface graphene leads to a more drastic increase in the compression of the top layer against the tip. In the supported case, existing substrate material (SiO_2) already compresses the tip against the top graphene layer. However, although individual silicon atoms are more attractive than carbon or oxygen atoms, graphene's higher density of atoms near the surface relative to SiO_2 results in a greater overall attraction of the tip atoms to the graphene surface. The addition of graphene layers thus enhances tip−sample adhesion and leads to slightly greater compression (force per area) of the top layer, even for the ideal, perfectly flat surfaces simulated here. The key observation in these calculations is the qualitative difference in the slope of the two curves in Figure 7b, as actual pressure values depend on the MD parameters used. In addition, results can vary depending on the assumptions made regarding surface structure,[37] as calculated attractive forces exerted by the Si_3N_4 or SiO_2 surface depend on the abundance of each atomic species at the interface. In the continuum model used here, we assumed that the surface distribution is the same as in the bulk.

Figure 7c shows the calculated membrane profiles for thicknesses ranging from one to three graphene layers under a 15 nN load applied by the tip. The more flexible monolayer membrane deflects more under a given load, as expected from the experiments. Its flexibility also results in a greater tendency of the graphene to conform to (wrap around) the tip about the point of contact. Figure 7d shows the calculated profiles for different numbers of layers at the maximum height each attained while being pulled upward by the tip. The corresponding applied loads were ≈−65 nN (monolayer), ≈−200 nN (bilayer), and ≈−300 nN (trilayer). Under this configuration, the membranes cannot conform well to the tip. However, conformation can occur for lower tip heights, as illustrated in Figure 7e for a monolayer membrane. Finally, Figure 7f shows the calculated tip−membrane contact force for different thicknesses as a function of a range of tip heights. At a given load, the membrane deflection increases for thinner membranes, particularly at higher loads, in qualitative agreement with variable-load topographical measurements (Supporting Information, Figure S5). The in-plane stiffness increases with layer number, as indicated by the fact that thicker membranes require higher loads to attain a given tip height.

4. DISCUSSION

4.1. Friction and Adhesion on Supported Graphene versus Bare SiO_2. The greater pull-off force observed for

dx.doi.org/10.1021/la304079a | *Langmuir* 2013, 29, 235−243

supported graphene in comparison with that for the bare SiO_2 surface was initially unexpected, as both the greater hydrophilicity and surface dipole of SiO_2 could lead to greater adhesion. Transition fits to the friction–load data indicate that graphene behaves more JKR-like than SiO_2, which can occur due to either greater surface compliance or stronger short-range adhesive forces.[33−35] We found that both phenomena play a role here: Graphene is more compliant than SiO_2, as it is adhered to the substrate only via nonbonded interactions. (A similar difference in compliance between SiO_2 and multilayer graphene was observed by Poot et al.[15]) Further, graphene has a much higher density of atoms near the surface. The magnitude of the pull-off force is thus enhanced by both the greater contact area at pull-off and the closer proximity of the surface atoms to the tip on supported graphene relative to bare SiO_2. Our force-per-area calculations for ideally flat infinite slabs also predict greater adhesive force on supported graphene, even though roughness and atomic structure were not considered.

We note that the lower rms roughness on supported graphene relative to bare SiO_2 indicates that it is not seamlessly adhered to the substrate, as predicted elsewhere.[38] Thus, there exist small gaps between the graphene and substrate[39,40] that can lead to or enhance differences in compliance. Ultimately, we found that the work of adhesion does not differ significantly between the SiO_2 and the supported monolayer graphene surfaces, despite any differences in surface chemistry. Although this result may come as a surprise, the work of adhesion may be similar due to a balancing effect between graphene's greater surface atom density on the one hand and the stronger interaction with individual surface atoms in SiO_2 (particularly Si) on the other. We believe this is compounded by the differences in atomic distribution along the direction normal to the surface, which affect the shape of the interaction, as follows.

A high work of adhesion can occur when a small attractive force is applied over a relatively long distance; likewise, a low work of adhesion can occur when a large force is applied over a short distance. Accordingly, the contrast between the work of adhesion and the pull-off force measurements (and pressure calculations) suggests that the effective tip–sample interaction potentials are of similar depth (adhesion energy) but differing slope (force) in the attractive regime. Thus, supported graphene exhibits an effectively narrower attractive well. We believe the more rapid decay of forces on graphene may be a consequence of the discontinuous nature between the graphene and subsurface material.[41] The top graphene layer (or layers), which dominate the attractive interactions with the AFM tip, are spaced from each other and from the substrate by relatively large distances (≈0.5 nm). In contrast, SiO_2 is more continuous, with atoms that are not localized at discrete depths, as in graphene (or graphene-on-SiO_2).

4.2. Multilayer Adhesion Contrast on Suspended versus Supported Graphene. The magnitude of the pull-off force varied in the following descending order: supported graphene, suspended multilayers, and suspended monolayers. The higher pull-off force on supported graphene results from the attraction of the tip to both surface and subsurface material. We note that a similar contribution of subsurface material has been observed recently in macroscopic adhesion measurements between gecko feet and SiO_2/Si substrates of varying SiO_2 thickness.[42] Further, attraction of graphene to SiO_2 limits the tip's ability to separate the graphene layers from the substrate, and though greater than for bare SiO_2, the contact area remains dominated by the tip–substrate interaction throughout the unloading process.

In the case of membranes, for a range of tip heights significantly lower than the maximum height attained, the simulations indicate that contact area can quickly increase upon contact. As the tip pulls upward on a membrane, contact area then decreases to a minimum at the maximum tip height (Figure 7e). The higher pull-off force with increasing layer number observed experimentally on suspended graphene is qualitatively consistent with the simulations (Figure 7d), for which the ratio of adhesive forces was 1:3:4.5 for monolayer/bilayer/trilayer. Although the maximum membrane heights did not differ significantly as a function of layer number, the required forces differed considerably because the in-plane stiffness scales approximately with the cube of graphene layer number (Figure 7f).[15,43] The reduced overall curvature of the thicker membranes also means that more of the membrane is close to the tip (Figure 7d). Further, as the number of layers increases, the tip can exert a greater attractive force on the membrane due to additional interactions between the tip and subsurface layers.

The simulated adhesive forces for membranes of different thickness show trends similar to what we observed in the experiments, with adhesive force increasing with layer number. However, the ratios between the measured values are significantly reduced with respect to the simulated values. We attribute this discrepancy primarily to the use of continuum approximations to model the membranes. This approach cannot reproduce the exact geometry of the individual graphene layers at the location closest to the tip, which governs the baseline adhesive force. Adhesive forces are strongly influenced both by the local curvature of each individual membrane layer, as well as by the ability of each layer to conform to the tip. The fact that the experimental pull-off force ratios are smaller suggests that the peak adhesive force may be dominated by the top graphene layer, which may separate from the other layers at the point of contact.

4.3. Friction as a Function of Graphene Layer Number. The decrease in friction with increasing number of layers for supported graphene has generally been attributed to variations in out-of-plane deformability.[7,8,21] In that context, Lee et al. found that rippling effects occur but diminish with thickness.[7,8] Our calculations reveal a slight increase in the contact pressure between the tip and the top layer for increasing layer number, which could be expected to lead to higher friction forces. The work of Lee et al. indicates otherwise and suggests that reduced rippling and roughness are the dominant effects. Conversely, the experiments performed here suggest that compressive pressure effects dominate for suspended graphene. The calculated compressive pressure between an idealized smooth tip and a graphene monolayer (Figure 7b) drops from approximately 300 MPa to 0 Pa when the substrate is removed. Despite any rippling that can occur for membranes (Figure 7e), the experiments reveal that friction decreases when the substrate is removed, suggesting that reduced pressure is the important effect at this scale.

The steep increase in contact pressure versus number of layers for the suspended case (Figure 7b) explains the increase in friction force with increasing number of layers under negative or slightly positive loads. However, as the load increases further, thicker membranes deform more slowly and retain a smoother profile with respect to thinner membranes (Figure 7c). In Figure 7c, the positively loaded monolayer membrane is more

dx.doi.org/10.1021/la304079a | Langmuir 2013, 29, 235−243

steeply inclined than the trilayer near the tip, and it can thus adhere farther up the tip shaft. Hence, we conclude that the reversal in friction contrast at high loads results from a transition to a contact regime where (i) larger deflections by thinner membranes in response to applied load lead to greater conformation to the tip and more material that must be displaced laterally and (ii) the subsurface layer contribution to the tip−membrane contact pressure decreases relative to the now elevated compressive stresses imposed by the tip.

Although recent MD simulations of small tips on suspended monolayer and multilayer graphene show friction−load plots that exhibit positive (upward) curvature,[44] that is, reversed with respect to the experimental work reported here, local membrane deformation profiles for the larger tips used in these experiments (>20 times the size of the simulated tips in ref 44) may be expected to exhibit much greater complexity than small tips or those with high aspect ratios. Subsurface-layer assisted conformation of the membrane to the tip, described by the larger-scale simulations here, could lead to variations in the plowing (indent or protrusion) asymmetry described in ref 44, as well as introduce additional terms in the equation for friction.

5. SUMMARY

Using AFM, we investigated adhesion and friction on supported and suspended graphene mechanically exfoliated onto pit-patterned SiO_2/Si substrates. We observed significantly lower friction on supported graphene relative to the bare SiO_2 surface, independent of tip size and material. We found that the higher tip−sample pull-off forces we observed for supported graphene relative to bare SiO_2 were a result of graphene's greater atomic density near the surface leading to higher short-range forces, as well as greater contact area arising from increased material compliance. Among the graphene structures, pull-off forces were greatest for supported graphene, followed by multilayer and monolayer membranes (suspended graphene). This trend is a combined result of in-plane membrane elasticity and van der Waals forces between the tip and surface layer and any substrate material or subsurface graphene layers. Finally, friction forces increased with increasing number of layers for suspended graphene at low or negative applied normal loads, in contrast to established trends observed for supported graphene. This result for membranes stems from a competition between local deformation of the graphene near the tip, the broader membrane geometry, and van der Waals forces that attract the tip to subsurface graphene layers.

■ ASSOCIATED CONTENT

Ⓢ Supporting Information

Experimental setup; optical and scanning electron microscopy images; Raman data; simulations setup; and membrane deflection. This material is available free of charge via the Internet at http://pubs.acs.org.

■ AUTHOR INFORMATION

Corresponding Author

*E-mail: rachel.cannara@nist.gov.

Notes

The authors declare no competing financial interest.

■ ACKNOWLEDGMENTS

The authors thank Fred Sharifi and Scott Bunch for helpful discussions. Z.D., N.N.K., and H.X. acknowledge support under the Cooperative Research Agreement between the University of Maryland and the National Institute of Standards and Technology Center for Nanoscale Science and Technology, award 70NANB10H193, through the University of Maryland. The U.S. National Science Foundation is gratefully acknowledged via grant CMMI-0841840 (S.D.S.) and grants CMMI-1069076 and CMMI-1129826 (T.L.)

■ REFERENCES

(1) Zhang, Y. B.; Tan, Y. W.; Stormer, H. L.; Kim, P. Experimental Observation of the Quantum Hall Effect and Berry's Phase in Graphene. *Nature* **2005**, *438*, 201−204.

(2) Castro Neto, A. H.; Guinea, F.; Peres, N. M. R.; Novoselov, K. S.; Geim, A. K. The Electronic Properties of Graphene. *Rev. Mod. Phys.* **2009**, *81*, 109−162.

(3) Balandin, A. A.; Ghosh, S.; Bao, W.; Calizo, I.; Teweldebrhan, D.; Miao, F.; Lau, C. N. Superior Thermal Conductivity of Single-Layer Graphene. *Nano Lett.* **2008**, *8*, 902−907.

(4) Ghosh, S.; Calizo, I.; Teweldebrhan, D.; Pokatilov, E. P.; Nika, D. L.; Balandin, A. A.; Bao, W.; Miao, F.; Lau, C. N. Extremely High Thermal Conductivity of Graphene: Prospects for Thermal Management Applications in Nanoelectronic Circuits. *Appl. Phys. Lett.* **2008**, *92* (151911), 3.

(5) Bunch, J. S.; van der Zande, A. M.; Verbridge, S. S.; Frank, I. W.; Tanenbaum, D. M.; Parpia, J. M.; Craighead, H. G.; McEuen, P. L. Electromechanical Resonators from Graphene Sheets. *Science* **2007**, *26*, 490−493.

(6) Lee, C.; Wei, X. D.; Kysar, J. W.; Hone, J. Measurement of the Elastic Properties and Intrinsic Strength of Monolayer Graphene. *Science* **2008**, *321*, 385−388.

(7) Lee, C.; Li, Q. Y.; Kalb, W.; Liu, X. Z.; Berger, H.; Carpick, R. W.; Hone, J. Frictional Characteristics of Atomically Thin Sheets. *Science* **2010**, *328*, 76−80.

(8) Li, Q.; Lee, C.; Carpick, R. W.; Hone, J. Substrate Effect on Thickness-Dependent Friction on Graphene. *Phys. Stat. Solidi B* **2010**, *247*, 2909−2914.

(9) Geim, A. K.; Novoselov, K. S. The Rise of Graphene. *Nat. Mater.* **2007**, *6*, 183−191.

(10) Geim, A. K. Graphene: Status and Prospects. *Science* **2009**, *324*, 1530−1534.

(11) Bekyarova, E.; Itkis, M. E.; Ramesh, P.; Berger, C.; Sprinkle, M.; de Heer, W. A.; Haddon, R. C. Chemical Modification of Epitaxial Graphene: Spontaneous Grafting of Aryl Groups. *J. Am. Chem. Soc.* **2009**, *131*, 1336−1337.

(12) Cervantes-Sodi, F.; Csanyi, G.; Piscanec, S.; Ferrari, A. C. Edge-Functionalized and Substitutionally Doped Graphene Nanoribbons: Electronic and Spin Properties. *Phys. Rev. B* **2008**, *77* (165427), 13.

(13) Kwon, S.; Ko, J.-H.; Jeon, K.-J.; Kim, Y.-H.; Park, J. Y. Enhanced Nanoscale Friction on Fluorinated Graphene. *Nano Lett.* **2012**, in press.

(14) Frank, I. W.; Tanenbaum, D. M.; van der Zande, A. M.; McEuen, P. L. Mechanical Properties of Suspended Graphene Sheets. *J. Vac. Sci. Technol. B* **2007**, *25*, 2558−2561.

(15) Poot, M.; van der Zant, H. S. J. Nanomechanical Properties of Few-Layer Graphene Membranes. *Appl. Phys. Lett.* **2008**, *92* (063111), 3.

(16) Lee, C.; Wei, X. D.; Li, Q. Y.; Carpick, R. W.; Kysar, J. W.; Hone, J. Elastic and Frictional Properties of Graphene. *Phys. Status Solidi B* **2009**, *246*, 2562−2567.

(17) Suk, J. W.; Piner, R. D.; An, J.; Ruoff, R. S. Mechanical Properties of Monolayer Graphene Oxide. *ACS Nano* **2010**, *4*, 6557−6560.

(18) Filleter, T.; McChesney, J. L.; Bostwick, A.; Rotenberg, E.; Emtsev, K. V.; Seyller, T.; Horn, K.; Bennewitz, R. Friction and

Dissipation in Epitaxial Graphene Films. *Phys. Rev. Lett.* **2009**, *102* (086102), 4.
(19) Filleter, T.; Bennewitz., R. Structural and Frictional Properties of Graphene Films on SiC(0001) Studied by Atomic Force Microscopy. *Phys. Rev. B* **2010**, *81* (155412), 7.
(20) Lee, H.; Lee, N.; Seo, Y.; Eom, J.; Lee, S. Comparison of Frictional Forces on Graphene and Graphite. *Nanotechnology* **2009**, *20* (325701), 6.
(21) Smolyanitsky, A.; Killgore, J. P.; Tewary, V. K. Effect of Elastic Deformation on Frictional Properties of Few-Layer Graphene. *Phys. Rev. B* **2012**, *85* (035412), 6.
(22) Choi, J. S.; Kim, J. S.; Byun, I. S.; Lee, D. H.; Lee, M. J.; Park, B. H.; Lee, C.; Yoon, D.; Cheong, H.; Lee, K. H.; Son, Y. W.; Park, J. Y.; Salmeron, M. Friction Anisotropy−Driven Domain Imaging on Exfoliated Monolayer Graphene. *Science* **2011**, *333*, 607−610.
(23) Ferrari, A. C.; Meyer, J. C.; Scardaci, V.; Casiraghi, C.; Lazzeri, M.; Mauri, F.; Piscanec, S.; Jiang, D.; Novoselov, K. S.; Roth, S.; Geim, A. K. Raman Spectrum of Graphene and Graphene Layers. *Phys. Rev. Lett.* **2006**, *97* (187401), 4.
(24) Ni, Z.; Wang, Y.; Yu, T.; Shen, Z. Raman Spectroscopy and Imaging of Graphene. *Nano Res.* **2008**, *1*, 273−291.
(25) Li, X.; Wang, X.; Zhang, L.; Lee, S.; Dai, H. Chemically Derived, Ultrasmooth Graphene Nanoribbon Semiconductors. *Science* **2008**, *319*, 1229−1232.
(26) Jiao, L.; Zhang, L.; Wang, X.; Diankov, G.; Dai, H. Narrow Graphene Nanoribbons from Carbon Nanotubes. *Nature* **2009**, *458*, 877−880.
(27) Cullen, W. G.; Yamamoto, M.; Burson, K. M.; Chen, J. H.; Jang, C.; Li, L.; Fuhrer, M. S.; Williams, E. D. High-Fidelity Conformation of Graphene to SiO_2 Topographic Features. *Phys. Rev. Lett.* **2010**, *105* (215504), 4.
(28) Li, T. Extrinsic Morphology of Graphene. *Modell. Simul. Mater. Sci. Eng.* **2011**, *19* (054005), 15.
(29) Li, T.; Zhang, Z. Substrate-Regulated Morphology of Graphene. *J. Phys. D: Appl. Phys.* **2010**, *43* (075303), 7.
(30) Maugis, D. Adhesion of Spheres: The JKR-DMT Transition Using a Dugdale Model. *J. Colloid Interface Sci.* **1992**, *150*, 243−269.
(31) Derjaguin, B. V.; Muller, V. M.; Toporov, Y. P. Effect of Contact Deformations on the Adhesion of Particles. *J. Colloid Interface Sci.* **1975**, *53*, 314−325.
(32) Johnson, K. L.; Kendall, K.; Roberts, A. D. Surface Energy and the Contact of Elastic Solids. *Proc. R. Soc. London, Ser. A* **1971**, *324*, 301−313.
(33) Carpick, R. W.; Ogletree, D. F.; Salmeron, M. A General Equation for Fitting Contact Area and Friction vs Load Measurements. *J. Colloid Interface Sci.* **1999**, *211*, 395−400.
(34) Grierson, D. S.; Flater, E. E.; Carpick, R. W. Accounting for the JKR−DMT Transition in Adhesion and Friction Measurements with Atomic Force Microscopy. *J. Adhes. Sci. Technol.* **2005**, *19*, 291−311.
(35) Schwarz, U. D. A Generalized Analytical Model for the Elastic Deformation of an Adhesive Contact between a Sphere and a Flat Surface. *J. Colloid Interface Sci.* **2003**, *261*, 99−106.
(36) Klimov, N. N.; Jung, S.; Zhu, S.; Li, T.; Wright, C. A.; Solares, S. D.; Newell, D. B.; Zhitenev, N. B.; Stroscio, J. A. Electromechanical Properties of Graphene Drumheads. *Science* **2012**, *336*, 1557−1561.
(37) Rappe, A. K.; Casewit, C. J.; Colwell, K. S.; Goddard, W. A.; Skiff, W. M. UFF, a Full Periodic Table Force Field for Molecular Mechanics and Molecular Dynamics Simulations. *J. Am. Chem. Soc.* **1992**, *114*, 10024−10035.
(38) Zhang, Z.; Li, T. Determining Graphene Adhesion via Substrate-Regulated Morphology of Graphene. *J. Appl. Phys.* **2011**, *110* (083526), 5.
(39) Scharfenberg, S.; Mansukhani, N.; Chialvo, C.; Weaver, R. L.; Mason, N. Observation of a Snap-Through Instability in Graphene. *Appl. Phys. Lett.* **2012**, *100* (021910), 3.
(40) Li, T.; Zhang, Z. Snap-Through Instability of Graphene on Substrates. *Nanoscale Res. Lett.* **2010**, *5*, 169−173.
(41) Israelachvili, J. N. *Intermolecular and Surface Forces*, 3rd ed.; Academic Press: Burlington, MA, 2011; p 710.
(42) Loskill, P.; Puthoff, J.; Wilkinson, M.; Mecke, K.; Jacobs, K.; Autumn, K. Macroscale Adhesion of Gecko Setae Reflects Nanoscale Differences in Subsurface Composition. *J. R. Soc. Interface* **2013**, *10*, 20120587.
(43) Timoshenko, S. *Theory of Plates and Shells*; McGraw-Hill Book Company: New York, 1940.
(44) Smolyanitsky, A.; Killgore, J. P. Anomalous Friction in Suspended Graphene. *Phys. Rev. B* **2012**, *86* (125432), 5.

SUPPORTING INFORMATION:

Nanoscale Interfacial Friction and Adhesion on Supported versus Suspended Monolayer and Multilayer Graphene

Zhao Deng,[1,2] Nikolai N. Klimov,[1,3] Santiago D. Solares,[2,4] Teng Li,[2,4] Hua Xu,[1,2] and Rachel J. Cannara[1*]

[1] *Center for Nanoscale Science and Technology, National Institute of Standards and Technology, Gaithersburg, MD 20899*

[2] *Maryland NanoCenter, University of Maryland, College Park, MD 20742*

[3] *Physical Measurement Laboratory, National Institute of Standards and Technology, Gaithersburg, MD 20899*

[4] *Department of Mechanical Engineering, University of Maryland, College Park, MD 20742*

S1. EXPERIMENTAL SETUP

Graphene samples were prepared via mechanical exfoliation of natural graphite onto silicon dioxide-on-silicon (SiO_2/Si) substrates,[S1] fabricated from Si wafers with a 300 nm-thick thermally-grown layer of SiO_2. An array of pits was formed on the SiO_2/Si wafers by reactive ion etching (RIE). The etch mask consisted of a 300 nm to 350 nm thick layer of photoresist spin-coated onto the SiO_2/Si wafers and baked for two minutes at 115 °C. The array pattern was transferred by photolithography from a photomask to the photoresist, which was then developed. The pit array was then obtained after a three to four minute RIE in O_2/CHF_3 radio frequency (RF) plasma with gas flow rates of 5 sccm O_2 and 45 sccm CHF_3 at a pressure of 50 mTorr (≈ 7 Pa) and 200 W RF power. After dissolving the photoresist, a protective layer of poly(methyl methacrylate) was spin-coated onto the wafers, which were then diced into multiple 14 mm × 14 mm chips. The substrates were then thoroughly cleaned in solvents and deionized water, followed by piranha (1:4 = 30% H_2O_2: 98% H_2SO_4) and oxygen plasma cleaning.

Figure S1 shows both optical and scanning electron microscope (SEM) images of patterned substrates with exfoliated graphene flakes. For the sample used in this study, SEM imaging was not performed in order to avoid contamination by the electron beam and thus permit future use. The dimensions of the pits were measured by atomic force microscopy (AFM) and found to be

cylindrical with a diameter of (1.60 ± 0.05) μm and a depth of 100 nm to 150 nm, depending on the etch time. The spacing between pits was (4.0 ± 0.1) μm. After the exfoliation and deposition process, graphene flakes averaging 10 μm to 20 μm in size were observed to span a range of pits, forming an array of suspended graphene (membranes). Some membranes collapsed to the floor of the pits, but many remained suspended and could thus be used in this study. Figure S2 shows Raman spectra (with an excitation wavelength of 514.5 nm) for the supported mono-, bi-, and trilayer graphene and for the monolayer/bilayer membrane in Figures 5 and 6 of the main text. For a given thickness, the Raman data were nominally identical when comparing supported *vs*. suspended graphene structures, consistent with previous work.[S2]

The AFM probes used in this study were: silicon (Si) with tip radius, R = (8 ± 2) nm; silicon nitride (Si_3N_4) with R = (15 ± 3) nm; and ultrananocrystalline diamond (UNCD) with R = (30 ± 5) nm). AFM tips were characterized using SEM to measure tip radius, and to check for any overall changes in tip shape by comparing SEM images before and after the experiments. All flexural spring constants were on the order of 0.1 N/m, as measured using the thermal noise method.[S3] The AFM measurements were performed at (30 ± 1) °C in dry nitrogen (< 1 % relative humidity), using the Si_3N_4 tip, unless otherwise stated. No discernable change in tip radius occurred during the experiment, based on the SEM images, as exemplified by the SEM images of the Si_3N_4 tip in Figure S3.

In an adhesive force measurement, the tip is first pressed into the sample during "approach," followed by a full separation of the tip and sample surface attained by pulling ("retracting") the sample away from the tip. Adhesive forces are proportional to the difference between the vertical signal at pull-off and its value when the tip is fully separated from the surface. Normal force calibration factors (in Newtons per Volt) were calculated by multiplying the flexural spring constant of the cantilever by the deflection sensitivity (slope of the vertical force-displacement curve) on a rigid surface (SiO_2/Si). Prior to each friction-load measurement, we acquired several vertical force-displacement curves to determine the range of applied normal loads to be used. Normal and lateral signals were then recorded while slowly ramping the load setpoint, where each line thus corresponded to a single nominal load value. Average friction forces were determined in the usual way by taking half of the difference between trace and retrace lateral signals, multiplied by a lateral force calibration factor calculated via the diamagnetic lateral force

calibration method.[S4] All friction-load curves were obtained over individual 10 nm scan lines at a scan speed of 40 nm/s. The force-displacement curves were performed at an approach and retract rate of 1 μm/s, and the effective rate for the friction-load measurements was ≈ 10 nm/s.

The experimental uncertainties correspond to one standard deviation of the measured value, unless otherwise noted.

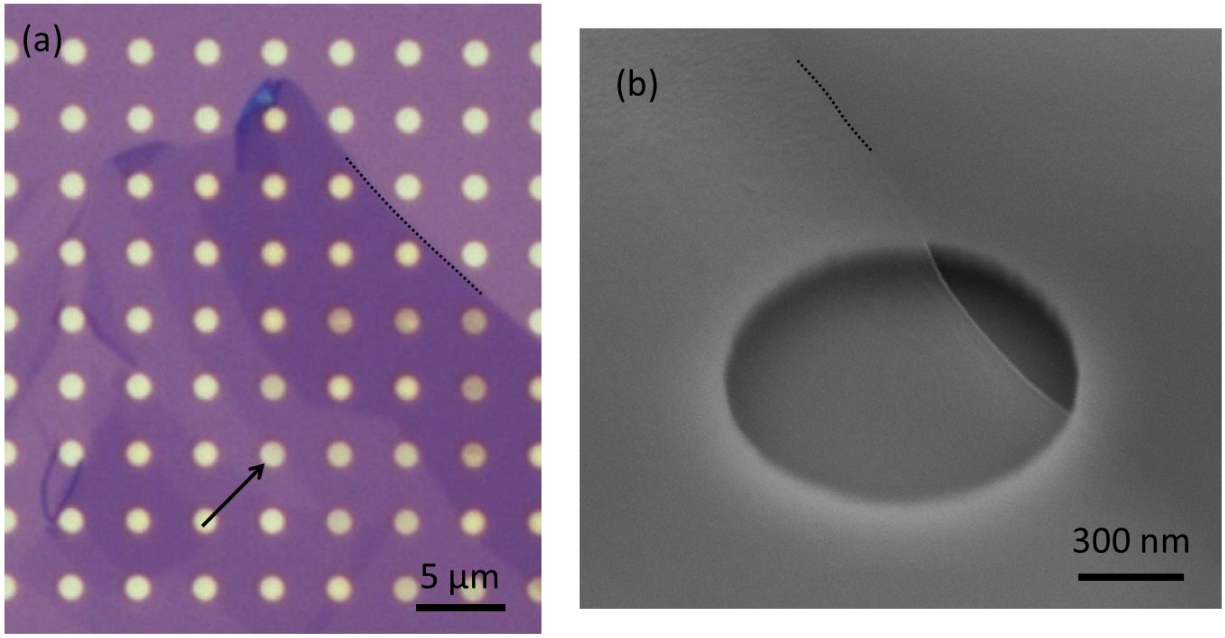

Figure S1. (a) An optical image of the pit-patterned SiO_2/Si surface with the exfoliated graphene flake; the arrow points to the pit shown in Figures 5a-5d and S2, and the dotted line indicates a boundary between bare SiO_2 surface and the flake. (b) An SEM image of a similarly prepared sample (but with 1 μm pits) showing that the graphene appears to adhere to the side walls of the pits, as shown more definitively by the AFM topography measurements. (SEM imaging on the sample in the main experiment was not performed in order to avoid contamination by the electron beam and thus permit future use.) The dotted line indicates the boundary between the graphene and bare substrate.

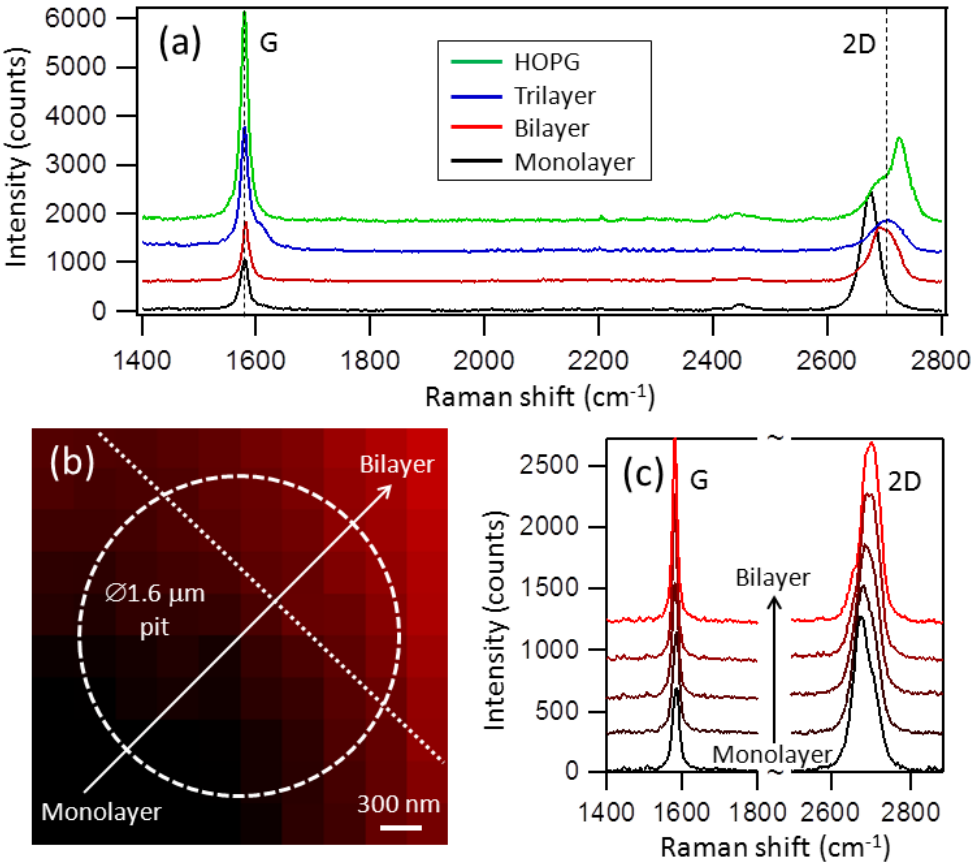

Figure S2. (a) Raman spectra for the monolayer, bilayer, and trilayer graphene regions in Figure 5 of the main text, including reference spectra for highly ordered pyrolitic graphite (HOPG). For clarity, each data set has been offset vertically. The G peak shifts downward, the 2D peak shifts upwards, and the 2D to G peak ratio decreases with increasing layer thickness. (b) Raman map of the monolayer/bilayer membrane. The dashed and dotted lines indicate the pit shape and location of the monolayer/bilayer graphene boundary, respectively. (c) Evolution of the Raman G and 2D peaks across the monolayer/bilayer graphene boundary traversing the pit, as measured along the direction indicated by the arrow in (b). Each data set has been offset vertically.

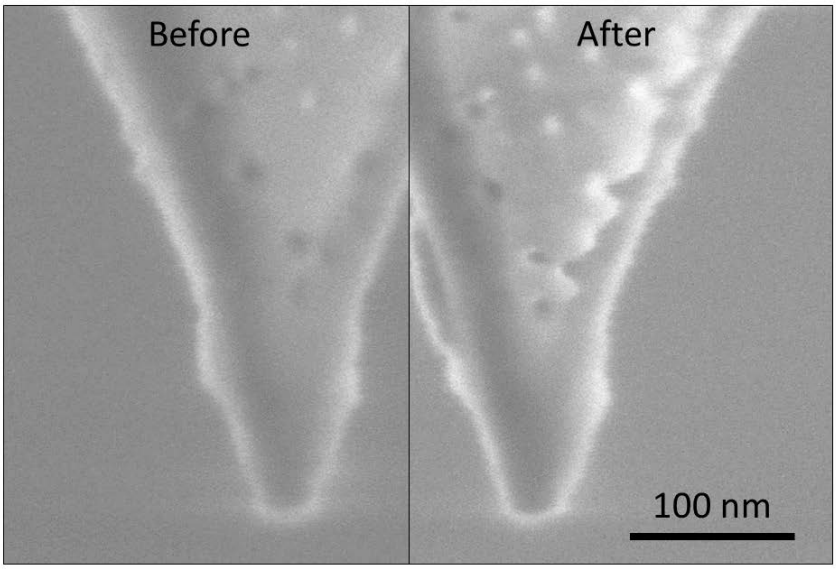

Figure S3. SEM images of the Si_3N_4 tip before and after the experiment. Despite some blurring due to charging in the SEM, we did not observe any significant tip wear or contamination from the experiment.

S2. SIMULATIONS SETUP

In the first set of simulations (Figure S4a), we calculated the pressure between an Si_3N_4 surface (the tip) and a graphene layer as a function of the number of subsurface graphene layers and the presence or absence of an SiO_2 substrate. We assumed the surfaces and graphene layers to be perfectly flat and infinite (*i.e.*, without surface roughness or atomic structure), and free to move only in the direction normal to the surface. They interacted with one another only via non-bonded (van der Waals and Pauli repulsion) forces, as described by Lennard-Jones type functions approximately fit to molecular dynamics (MD) non-bonded interaction parameters.[S5] For each case, we constructed a set of equations describing the forces exerted on each structure (tip, substrate, and individual graphene layers) by all other structures, as a function of individual position. We then relaxed the system in the vertical direction through a numerical implementation of the steepest descent geometry optimization algorithm[S6] until the net force acting on each structure vanished. Finally, we calculated the contact pressure between the Si_3N_4 surface and the top graphene layer using the appropriate Lennard-Jones function.

In the second set of simulations (Figure S4b), we constructed an axisymmetric continuum-sheet model of a 1.6 μm-diameter clamped circular graphene membrane interacting with a 15 nm-radius Si_3N_4 sphere (AFM tip). The interaction between the tip and each element of the membrane was described by Lennard-Jones-type functions fit to MD non-bonded parameters through integration of the interaction forces over the volume of the sphere and the area of the membrane.[S5] The elastic deformation of the membrane was described by an area energy term for the stretching or compression of each concentric element of the membrane (Figure S4b) based on a fit to MD calculations of isotropic areal deformation of a two-dimensional graphene sheet.[S7] A "bending" term was included to describe the change in membrane slope for adjacent membrane elements (side view in Figure S4b) and was approximately fit to atomistic calculations of a graphene sheet bent by varying angles.[S7] A set of equations was set up describing the energy of the system as a function of the position of the tip and the border of each areal element, from which the forces acting on each coordinate could be obtained. The equations were then applied to membranes of different numbers of layers (n = 1, 2 and 3) pushed down or pulled up by the AFM tip. In each case, we numerically calculated the relaxed membrane profile at different tip heights using the steepest descent geometry optimization algorithm[S6] and extracted the corresponding tip-membrane interaction force.

The main purpose of these calculations is to obtain physical insight regarding general trends in the behavior of these graphene systems. The different quantities calculated are not necessarily quantitatively accurate, as they rely on a number of approximations: the treatment of graphene as a continuum material, the simplicity of the energy functions used, and the use of MD parameters from force fields that were not developed for our specific application. These assumptions can result in uncertainties that are in the worst case of the same order of magnitude as the measured quantity, depending on the type of calculation; however, the resulting errors are systematic and relative comparisons remain valid.

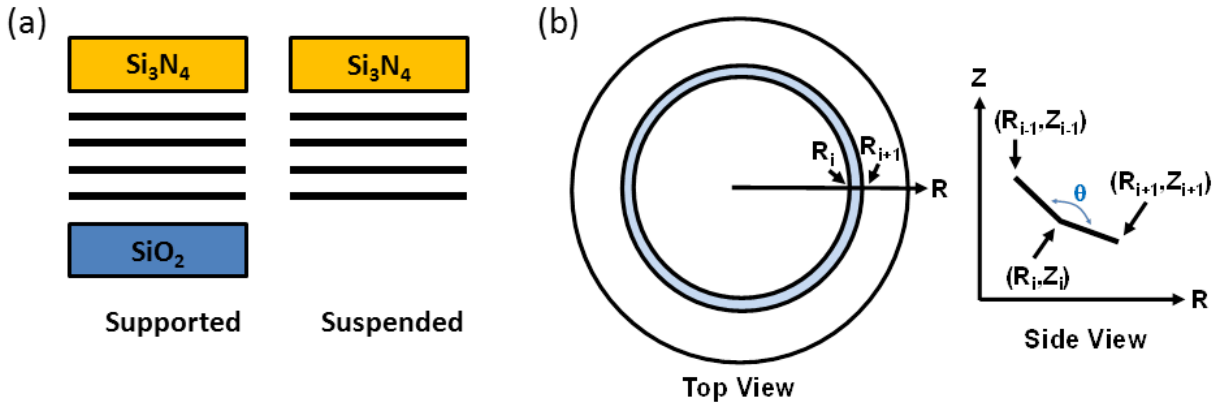

Figure S4. (a) Schematic of the van der Waals interaction model used for calculating the pressure between the top layer and the AFM tip for supported and suspended graphene. SiO_2 and Si_3N_4 denote the silicon dioxide substrate and silicon nitride AFM tip, respectively. (b) Schematic of the continuum membrane model used to calculate the profile of suspended graphene interacting with the AFM tip.

S3. VARIABLE-LOAD TOPOGRAPHY ON MEMBRANES

To confirm the variation in membrane height as a function of the normal load applied by an AFM tip, we performed variable-load topographical imaging of single-thickness graphene membranes. Figure S5 shows a comparison of membrane deflection (akin to "tip height" in Figure 7f) versus load for monolayer versus bilayer membranes. As expected (and as indicated separately by the slope maps in Figures 5c and 5g in the main text), the bilayer deflects less than the monolayer under a given load. Here, we used a very stiff cantilever in order to achieve high loads, which help demonstrate the overall trend in deflection at the center of the membrane, as a function of point loading for the different membrane thicknesses. We note that fitting each of the plots in Figure S5b to an established stress-strain equation[S8] yielded two-dimensional (2-D) prestress and 2-D Young's moduli consistent with literature values [S8,S9] (see Table S1).

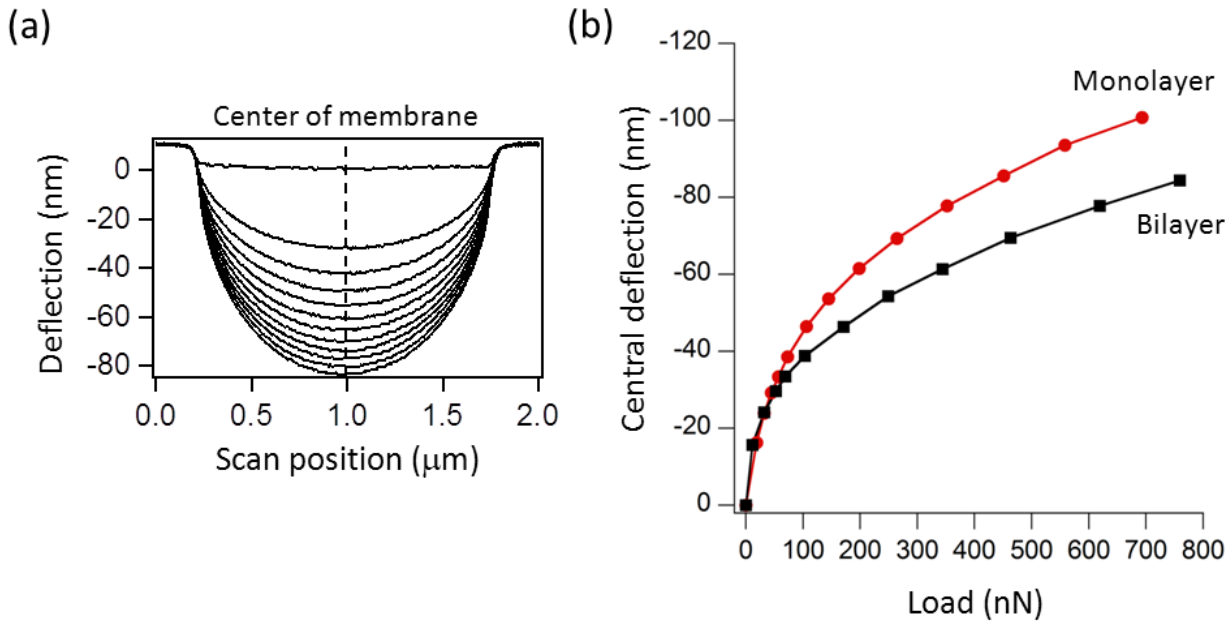

Figure S5. Deflection as a function of applied load for suspended monolayer and bilayer graphene membranes (each comprised of a single thickness—either one or two layers). (a) Deflection of a suspended bilayer, as measured along the central cross-sectional line of the membrane; the height of the deflection profile increases in overall magnitude with increasing load. (b) Deflection at the center of the membrane (dashed line shown in (a)) for the two different membranes, showing that the thicker membrane deflects less at a given load, as is most apparent at higher loads. The same Si cantilever with a normal spring constant of ≈ 1 N/m was used in both cases. Solid lines are visual guides connecting consecutive data points.

Table S1. 2-D prestress (σ^{2D}), 2-D Young's modulus (E^{2D}), and estimated Young's modulus (E) for monolayer (ML) and bilayer (BL) membranes. To obtain E, we used thicknesses, t, where t_{ML} = 0.335 nm and $t_{BL} = 2t_{ML}$, for consistency with Refs. S8 and S9. However, we use the unrounded value for q in Equation (2) of Ref. S8, which leads to differences with their reported values on the order of 10 %.

	σ^{2D} (N/m)	E^{2D} (N/m)	$E = E^{2D}/t$ (TPa)	E^{2D} (N/m) from Refs. S8, S9
ML membrane	0.38 ± 0.03	374 ± 10	1.12 ± 0.03	342 ± 30[S8]
BL membrane	0.46 ± 0.03	740 ± 20	1.10 ± 0.03	698[S9]

SUPPORTING INFORMATION REFERENCES

(S1) Novoselov, K. S.; Geim, A. K.; Morozov, S. V.; Jiang, D.; Zhang, Y.; Dubonos, S. V.; Grigorieva, I.V.; Firsov, A. A. Electric Field Effect in Atomically Thin Carbon Films. *Science* **2004**, *306*, 666-669.

(S2) Ferrari, A. C.; Meyer, J. C.; Scardaci, V.; Casiraghi, C.; Lazzeri, M.; Mauri, F.; Piscanec, S.; Jiang, D.; Novoselov, K. S.; Roth, S.; Geim, A. K. Raman Spectrum of Graphene and Graphene Layers. *Phys. Rev. Lett*. **2006**, *97*, 187401 (4pp).

(S3) Hutter, J. L.; Bechhoefer, J. Calibration of Atomic-Force Microscope Tips. *Rev. Sci. Instrum*. **1993**, *64*, 1868-1873.

(S4) Li, Q.; Kim, K. S.; Rydberg, A. Lateral Force Calibration of an Atomic Force Microscope with a Diamagnetic Levitation Spring System. *Rev. Sci. Instrum*. **2006**, *77*, 065105 (13pp).

(S5) Rappe, A. K.; Casewit, C. J.; Colwell, K. S.; Goddard, W. A.; Skiff, W. M. UFF, a Full Periodic Table Force Field for Molecular Mechanics and Molecular Dynamics Simulations. *J. Am. Chem. Soc*. **1992**, *114*, 10024-10035.

(S6) Leach, A. R. Molecular Modeling – Principles and Applications. 2nd Ed., Pearson Education Ltd. **2001**.

(S7) Stuart, S. J.; Tutein, A. B.; Harrison, J. A. A Reactive Potential for Hydrocarbons with Intermolecular Interactions. *J. Chem. Phys*. **2000**, *112*, 6472 (15pp).

(S8) Lee, C.; Wei, X. D.; Kysar, J. W.; Hone, J. Measurement of the Elastic Properties and Intrinsic Strength of Monolayer Graphene. *Science* **2008**, *321*, 385-388.

(S9) Lee, C.; Wei, X. D.; Li, Q.; Carpick, R. W.; Kysar, J. W.; Hone, J. Elastic and Frictional Properies of Graphene. *Phys. Status Solidi B* **2009**, *246*, 2562-2567.